Estimation of Unmodeled Forces on a Low-Thrust Space Vehicle

B. D. Tapley* and H. Hagar†
University of Texas at Austin, Austin, Texas

The application of a sequential estimation algorithm, which compensates for random errors in the dynamic model, to the problem of estimating the state of a continuously thrusting solar electric propulsion space vehicle is investigated. The dynamic model errors, due to random anomalies in the propulsion system, are approximated successfully by both first order and second order Gauss-Markov processes to obtain a more accurate and stable orbit determination algorithm. The importance of correct dynamic and measurement modeling in achieving accurate estimates is demonstrated.

I. Introduction

ERRORS due to unmodeled forces present one of the fundamental limitations on the navigation accuracy for the continuously thrusting solar-electric propulsion (SEP) spacecraft. The effects of the various error sources on the navigation accuracy are discussed in Refs. 1-3. For the SEP vehicle, the primary error source will be due to anomalies in the thrust program. Since the thrust is applied continuously, throughout the mission, small anomalies have time to cause significant terminal errors. Reference 1 points out the need for alternate orbit determination procedures, to the conventional least squares methods used for most interplanetary missions, if acceptable navigation accuracy is to be obtained during a SEP mission. Since the unmodeled accelerations due to the errors in the mathematical model will vary with time, compensation for the effect of the errors can be implemented in a direct manner by using a sequential, or Kalman-Bucy,[4] filter. Furthermore, if the extended form[5] of the sequential estimation algorithm is used, then the errors due to linearization assumptions will be minimized. The effect of model errors on the sequential estimation algorithm leads to the phenomenon of filter divergence.[6] The filter divergence can be delayed and, in some cases, prevented by the addition of a state noise covariance matrix to the equation for propagating the state error covariance matrix. The objective of this addition is to maintain filter reliability, in some suboptimal manner, by preventing the state error covariance matrix, and hence the observation residual weighting matrix (or Kalman gain), from vanishing. In Ref. 7, an alternate procedure is presented in which the unmodeled accelerations are approximated by a first-order Gauss-Markov process. The values of the unmodeled accelerations are estimated simultaneously with the values of the spacecraft position and velocity, and the estimated values of the unmodeled accelerations are used to improve the state propagation accuracy. Application of the algorithm to the problem of processing data from the Lunar Orbit phase of the Apollo 10 and 11 missions indicate that the algorithm yields a significant improvement in the orbit determination accuracy over that obtained with either the classical batch or Kalman-Bucy estimation algorithms.[8] Furthermore, in Refs. 8 and 9, the results of numerical simulations are presented which indicate that the estimates of the unmodeled accelerations provide an accurate representation of the true values of the unmodeled accelerations due to errors in either the earth or the lunar gravitational potential. Reference 10 discusses the general application of the method to the orbit determination problem for the Solar Electric Propulsion (SEP) mission.

In the subsequent discussion, the sequential estimation algorithm employing various model error compensation techniques is applied to the problem of estimating the state of a SEP space vehicle on an asteroid flyby mission. The performance of the model compensation algorithms in the presence of propulsion thrust anomalies is compared with the performance of both the uncompensated and state-noise compensated filters by numerical simulation.

II. Problem Statement

The problem considered is that of estimating the trajectory of a continuous low-thrust, solar-electric spacecraft subject to time correlated errors in the thrust acceleration vector. The nominal mission is initiated at escape from the earth's sphere of influence and terminates with a flyby of the asteroid Eros. Encounter with Eros occurs at a distance of 1.45 a.u., 152 days after heliocentric injection.

If only the central force attraction of the sun is included, the equations of motion for the SEP spacecraft can be expressed as

$$\dot{r}=v,\ \dot{v}=-(\mu/|r|^3)\ r+T \tag{1}$$

where, as shown in Fig. 1, r is a 3-vector of heliocentric position components, X, Y, Z; v is a 3-vector of heliocentric velocity components, $\dot{X}, \dot{Y}, \dot{Z}$; $|r|$ is the magnitude of r; and μ is the gravitational parameter of the sun. The heliocentric thrust acceleration T is composed of the design thrust acceleration T^* as well as the thrust acceleration errors from a number of sources such as beam voltage and current, grid warpage, deadband control errors, etc.[1] The heliocentric components of T, $[T_X T_Y T_Z]$, may be expressed in terms of components in a vehicle-centered frame, $[T_x T_y T_z]$, by the following relations:

$$\begin{bmatrix} T_X \\ T_Y \\ T_Z \end{bmatrix} = R \begin{bmatrix} T_x \\ T_y \\ T_z \end{bmatrix} \tag{2}$$

where

$$R \equiv \begin{bmatrix} \cos\psi & -\sin\psi & 0 \\ \sin\psi & \cos\psi & 0 \\ 0 & 0 & 1 \end{bmatrix}$$

Received May 3, 1974; revision received April 4, 1975. This investigation was supported under Grant AFOSR 72-2233 and by the Jet Propulsion Laboratory under Contract 953147.

Index categories: Navigation, Control, and Guidance Theory; Spacecraft Mission Studies and Economics; Spacecraft Tracking.

*Professor and Chairman, Department of Aerospace Engineering and Engineering Mechanics. Member AIAA.

†Formerly Research Engineer, Department of Aerospace Engineering and Engineering Mechanics. Member AIAA.

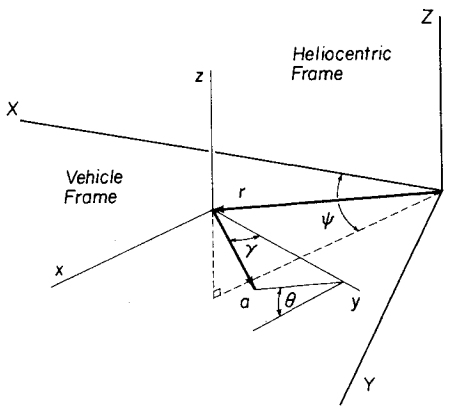

Fig. 1 Reference coordinates.

and where ψ is the heliocentric orientation angle (see Fig. 1). The vehicle-centered frame is oriented such that the x-y plane is parallel to the heliocentric X-Y plane, and the x-z plane remains parallel to the position vector, r.

The thrust components in the vehicle-centered reference frame are assumed to be expressed as follows:

$$\begin{bmatrix} T_x \\ T_y \\ T_z \end{bmatrix} = a \begin{bmatrix} \sin\gamma\cos\theta \\ \cos\gamma \\ \sin\gamma\sin\theta \end{bmatrix} \tag{3}$$

where a is the magnitude of the acceleration while γ and θ are the thrust vector orientation angles, as shown in Fig. 1. In the following study, it is assumed that

$$a = a^* + m_a \tag{4a}$$

$$\gamma = \gamma^* + m_\gamma \tag{4b}$$

$$\theta = \theta^* + m_\theta \tag{4c}$$

where a^*, γ^*, and θ^* represent the design or nominal values for the acceleration magnitude and the thrust pointing angles. The values of a^*, γ^* and θ^* are selected so that the design thrust T^* lies along vehicle-centered y-axis i.e., the design thrust will be normal to the position vector at all times. The quantities m_a, m_γ, and m_θ represent random errors in the values which characterize the design or nominal mission and lead to what will be referred to as the dynamic model error. The largest error, m_a, is usually autocorrelated.

III. Models for Error Compensation

In the following discussion, an estimation procedure is described in which the effects of the error in the thrust magnitude and in the thrust orientation angles are compensated for by using the general dynamic model compensation technique proposed in Ref. 7. In this approach, the thrust is separated into two components: modeled components and components due to errors, i.e.,

$$T = T^* + m \tag{5}$$

where T^* represents the modeled acceleration components and where m is a 3-vector of thrust error components. In the dynamic model compensation approach, the thrust errors, $m(t)$, are approximated by $\epsilon(t)$, where $\epsilon(t)$ is assumed to satisfy one of several possible first-order or second-order differential equations. The approximating differential equations for $\epsilon(t)$ are adjoined to Eq. (1) to obtain the state equations. The values of $\epsilon(t)$ and any unsepcified parameters in the differential equations which describe $\epsilon(t)$ are estimated simultaneously with the position and velocity components. The estimated values of ϵ_k at a time t_k are used to improve the predicted value of the position and velocity at the next observation time, t_{k+1}. In this investigation, models of three different orders are used to compensate for $m(t)$. The models are now described.

Model 0

In this model an arbitrary state noise covariance matrix, Q, is added to the differential equation governing the state error covariance. The Q-matrix compensates for the dynamic process noise and maintains a positive definite state error covariance matrix. The differential equations for the state vector, $\chi^T = [r^T v^T]$, are approximated by

$$\dot{r} = v, \quad \dot{v} = -\frac{\mu}{|r|^3} r + T^* + Ru \tag{6}$$

where r and v have been defined previously, and u is a random 3-vector with the a priori statistics $E\{u\} = 0$, $E\{u(t)u^T(\tau)\} = U(t)\delta(t-\tau)$, thus, this approach is equivalent to the assumption that $m(t)$ can be approximated as a zero-mean random process whose covariance matrix is $q(t) = R(t)U(t)R^T(t)$.

Model 1

In the first-order model, the thrust acceleration component along the vehicle y-axis is approximated by a first-order Gauss-Markov process. This component of error normally is the largest, and corresponds, approximately, to the magnitude of the thrust acceleration error. The x- and z-components are assumed to be purely random processes. Note that these components could be modeled also as a Gauss-Markov process; however, modeling only the y-component as such is computationally less demanding (by a factor of 3) than similar modeling for all three. The differential equations for the state vector, $\chi^T = [r^T v^T \epsilon \beta]$, are given as follows:

$$\dot{r} = v, \quad \dot{v} = -(\mu/|r|^3)r + T^* + R \begin{bmatrix} u_x \\ \epsilon \\ u_z \end{bmatrix} \tag{7}$$

with the addition of one of the following two assumptions:

$$\dot{\epsilon} = u_\epsilon \tag{8a}$$

or

$$\dot{\epsilon} = -\beta\epsilon + u_\epsilon, \qquad \dot{\beta} = u_\beta \tag{8b}$$

where u_x, u_z, u_ϵ, and u_β are random processes that satisfy the a priori statistical conditions:

$$E\{u_i\} = 0, \qquad E\{u_i^2\} = q_i, \qquad \ell \epsilon \{x, z, \epsilon, \beta\} \tag{9}$$

Model 2

For this model, the thrust acceleration error component along the vehicle y-axis is approximated by a second-order Gauss-Markov process. Again the same motivation for the modeling of only the y-component prevails as for Model 1. The x- and z-components again are treated as purely random processes. The differential equations for the state vector, $\chi^T = [r^T v^T \epsilon\ \eta\ \beta)$, are:

$$\dot{r} = v, \quad \dot{v} = -(\mu/|r|^3)r + T^* + R \begin{bmatrix} u_x \\ \epsilon \\ u_z \end{bmatrix}; \quad \dot{\epsilon} = \eta \tag{10}$$

in combination with one of the following two configurations:

$$\dot{\eta} = u_\eta \tag{11a}$$

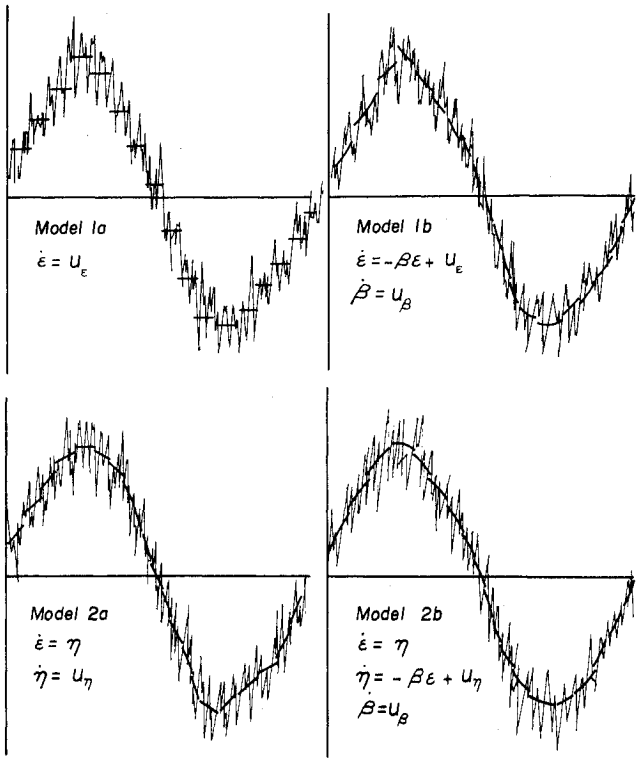

Fig. 2 Models for approximating the unmodeled accelerations.

or

$$\dot{\eta} = -\beta\epsilon + u_\eta \qquad \dot{\beta} = u_\beta \tag{11b}$$

where u_x, u_z, u_η, and u_β are random processes with a priori statistics

$$E\{u_\ell\} = 0, \qquad E\{u_\ell^2\} = q_\ell, \qquad \ell \epsilon \{x, z, \eta, \beta\} \tag{12}$$

Note that the state noise, or Q-matrix, compensated model, Model 0, does not allow an estimate of $m(t)$, for improving the accuracy of the propagation of the estimate, while each of Models 1 and 2 do. The concept represented by each of the models is illustrated in Fig. 2. Here, the light lines represent the actual error in the thrust acceleration magnitude. The dark line segments are gross representations of the approximated error. The discontinuities of these segments occur because at each observation time the estimation process provides new estimates which, in general, are not continuous. That is, the estimate of the function which approximates the unmodeled accelerations will change at each observation time. Note that Model 1a approximates the unmodeled acceleration by a sequence of horizontal lines, 2a by a sequence of straight lines, 1b by a sequence of exponentially increasing or decreasing functions and Model 2b by a sequence of sinusoidal functions. Estimation of the parameter β, adjusts the particular function in question to obtain the best local fit of the unmodeled accelerations. If the differential equations, which define either of the models described above, are adjoined to Eqs. (1), the equation of state can be expressed as

$$\dot{\chi} = F(\chi, t), \qquad \chi(t_o) = \chi_o \tag{13}$$

where χ includes both the position and velocity components as well as the quantities in the appropriate model for the error compensation.

The observations available for the orbit determination process are assumed to consist of the range-rate $\dot{\rho}$ measurements from Earth-based tracking stations and the onboard measurements of the angle λ between the directions to the Earth, and a specified navigation star. If each observation, specified generically as Ω, is made at the discrete times t_i, the nonlinear observation-state relationship can be expressed by

$$\Omega_i = G(\chi_i, t_i) + \nu_{\Omega i} \tag{14}$$

The observation error $\nu_{\Omega i}$ is assumed to have the a priori statistics $E\{\nu_{\Omega i}\} = 0$, $E\{\nu_{\Omega i}\nu_{\Omega j}\} = R_{\Omega i}\delta_{ij}$ where δ_{ij} is the Kronecker delta.

In the following investigation, the extended form of the Kalman-Bucy filter is used to obtain the state estimate.[5] That is, given an estimate $\hat{\chi}_{k-1}$, the associated state error covariance matrix P_{k-1}, and an observation Ω_k at the time t_k, then the estimate $\hat{\chi}$ and the state error covariance P_k at time t_k are obtained from the following equations:

$$\bar{\chi}_k = \hat{\chi}_{k-1} + \int_{t_{k-1}}^{t_k} F(\bar{\chi}(\tau), \tau)\, d\tau \tag{15a}$$

$$\bar{P}_k = P_{k-1} + \int_{t_{k-1}}^{t_k} \dot{\bar{P}}(\tau)\, d\tau \tag{15b}$$

$$\dot{\bar{P}} = A(t)\bar{P} + \bar{P}A^T(t) + Q(t) \tag{15c}$$

$$K_k = \bar{P}_k H_k^T [H_k \bar{P}_k H_k^T + R_{\Omega k}]^{-1} \tag{15d}$$

$$\hat{\chi}_k = \bar{\chi}_k + K_k[\Omega_k - G(\bar{\chi}_k, t_k)] \tag{15e}$$

$$P_k = [I - K_k H_k]\bar{P}_k \tag{15f}$$

where $F(\bar{\chi}, t)$ is the vector function representing the time derivative of χ, and where $A(t) = [\partial F(\chi, t)/\partial\chi]$, $H_k = [\partial G(\bar{\chi}_k, t_k)/\partial\chi]$, and Q is the complete state noise covariance matrix composed of zero and nonzero submatrices. These nonzero submatrices are denoted as Q', where $Q' \epsilon (q, q_\epsilon, q_\eta, q_\beta)$ as appropriate for the particular error model being used.

IV. Simulation Procedure

As previously indicated, errors are assumed to occur in both the magnitude of the thrust acceleration a as well as in the thrust vector pointing angles, γ and θ (see Fig. 1). For the design mission, the nominal thrust acceleration vector, T^*, is assumed to be of constant magnitude along the vehicle y-axis. Hence,

$$T^{*T} = a^*[-\sin\psi : \cos\psi : 0] \tag{16}$$

and therefore, the normal values of the pointing angles, γ and θ, are zero.

For the simulation process, the thrust acceleration error magnitude, m_a, is modeled by the random process, $m_a = m_{ao} \sin \omega t + u_a$, where m_{ao} and ω are representative parameters specified for the simulation (see Table 1). The random variable, u_a, has the statistics, $E[u_a] = 0$, and $E\{u_a^2\} = \sigma_a^2$.

In the thrust acceleration error simulation, the instantaneous values of the pointing angles γ and θ are assumed to be related as shown in Fig. 3. In this figure, the radius of the circle is the projection of the unit thrust vector on the vehicle-centered x-z plane. The circle represents the approximate boundary for the maximum pointing error of the thrust vector. Thus assuming a maximum pointing error of small angle $\bar{\gamma}$, the actual thrust vector describes a conical region of half angle $\bar{\gamma}$, and the radius of the boundary circle is $\sin\bar{\gamma} \approx \bar{\gamma}$.

The quantity $d = s(t - t_b)$ is the approximate path followed by the projection of the thrust onto the vehicle-centered x-z plane, since the last time t_b, that the maximum pointing error $\bar{\gamma}$ occurred. The scalar s represents a constant drift rate and t is the current mission time.

Table 1 Nominal mission and simulation parameters

Initial conditions		Initial uncertainties	Thurst acceleration error simulation
X	0.1505×10^9 km	10^4 km	$m_{a0}=6\%\ a^*=1.8\times10^{-2}$ mm/sec^2
Y	0. km	10^4 km	$\sigma_a=0.6\%\ a^*=1.8\times10^{-3}$ mm/sec^2
Z	−6378. km	10^4 km	$s=0.6\times10^{-6}$ rad/sec, $\sigma_s=0.24\times10^{-7}$ rad/sec
$\dot{X}$	0. m/sec	10^3 m/sec	$\sigma_\gamma=\sigma_\theta=0.001$ rad, $\sigma_\phi=0.91$ rad
$\dot{Y}$	31,743 m/sec	10^3 m/sec	$\bar{\gamma}=0.01745$ rad, $\omega=0.12\times10^{-5}$ Hz
$\dot{Z}$	73.8 m/sec	10^3 m/sec	Period of $\delta\alpha=2\pi/\omega=9.65$ days

Observation variances	Nominal thrust acceleration
$R_{\dot\rho}=(0.5$ mm/sec$)^2$ @ 1 min intervals	$\ddot{x}=\ddot{z}=0$ mm/sec^2
$R_\lambda=(7$ arsec$)^2$ @ 10 min intervals	$\ddot{y}=a^*=0.3$ mm/sec^2
Observation interval, $\Delta t=50$ min	(Orbital reference)

Tracking station	Longitude	Latitude	Constants
Woomera (JPL-41)	136°53′ 14″	−31° 22′ 55″	$\mu_{sun}=0.1327\times10^{12}$ km^3/sec^2
Goldstone (JPL-14)	243° 06′ 37″	35° 25′ 33″	$\omega_e=0.199\times10^{-6}$ rad/sec
Madrid (JPL-61)	355° 45′ 45′ 3″	40° 25′ 44″	

Navigation star unit vector elements: $\hat{s}=0.5538, 0.7384, 0.3846$ (heliocentric coordinates)

The angle ϕ, is sampled from a uniform distribution of zero mean and variance, $\sigma_\phi^2=0.828$. In addition, to provide a more realistic simulation, zero mean, purely random components are added to s, γ, and θ; their standard deviations are given in Table 1. The logic for simulating γ and θ is diagramed in Fig. 4; reference to Fig. 3 will aid in understanding the step-by-step sequence. The subscripts on the variables correspond to the discrete times at which the values are determined. Figure 5 illustrates a typical motion of the tip of the thrust vector projected on the x-z plane as determined by this simulation procedure over a period of 35 days. Note the approximately circular bound of radius $\simeq0.005$ mm/sec^2. Furthermore, the errors are seen to be somewhat concentrated in the first quadrant, and rather less dense in the fourth quadrant. As the simulation time continues beyond the 35 days shown here, one can expect that these errors would be more uniformly distributed within the full region. Figure 6 shows the error components along each of the orbital frame axes as functions of time. Note the periodicity of the y-component and the irregularity of the x- and z-components. Further, the y-component is approximately three times as large as the other components.

The structure of this simulation model, and hence its validity, is derived from consideration of the various thrust acceleration error sources encountered for SEP.[1] Sources such as beam voltage and current generally have low-frequency, time-varying error components which are manifested as such in the thrust acceleration error magnitude. Pointing errors in the thrust vector are heavily dominated by deadband errors. While the directional changes of deadband pointing errors (represented by ϕ) tend to be correlated, incomplete information on the physical nature of these errors suggest the choice of purely random, uniformly distributed directional changes as a conservative simulation technique.

The range-rate ($\dot\rho$) and star-vehicle-Earth angle (λ) observation errors are simulated by adding zero-mean Gaussian noise components to the actual observations, which are computed by using simulated true vehicle position and velocity. These random components are obtained by sampling from known Gaussian distributions. To study only the effects of modeling errors, the true and assumed observation error variances are chosen to be identical: $\sigma_{\dot\rho}=0.5$ mm/sec for one minute observation intervals; $\sigma_\lambda=7$ arcsec for 10 min observation intervals.

V. Numerical Results

Numerical experiments were carried out to assess the orbit determination performance of each of the models in compensating for the simulated thrust acceleration errors described. In performing the various numerical simulations, a common set of basic problem data is used consistently. This approach provides a common basis for evaluating the estimation performance of each of the approximating models. This set of data is given in Table 1. The initial conditions, position and velocity, are the same for both the simulated and nominal trajectories. The initial geometry is such that the Greenwich Meridian intersects the X-axis at midnight, GMT,

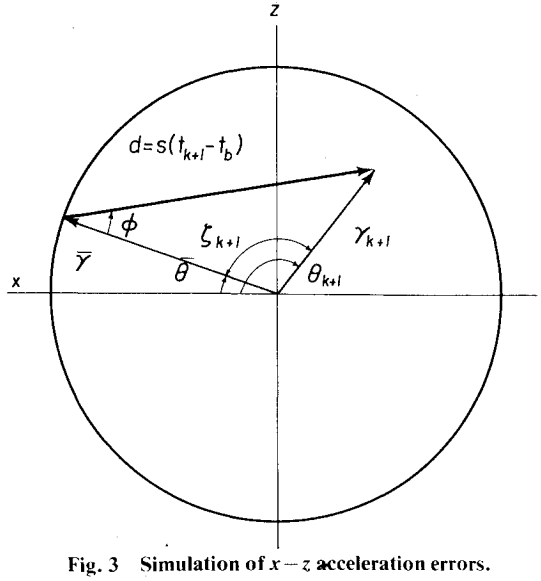

Fig. 3 Simulation of $x-z$ acceleration errors.

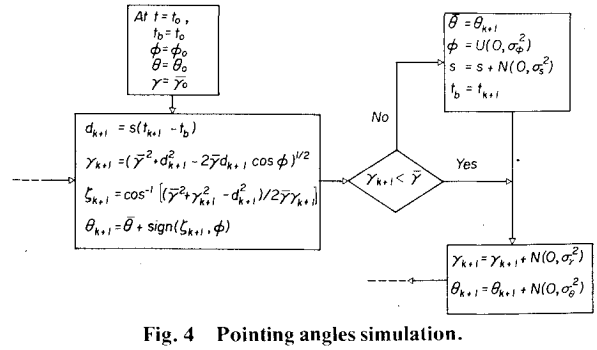

Fig. 4 Pointing angles simulation.

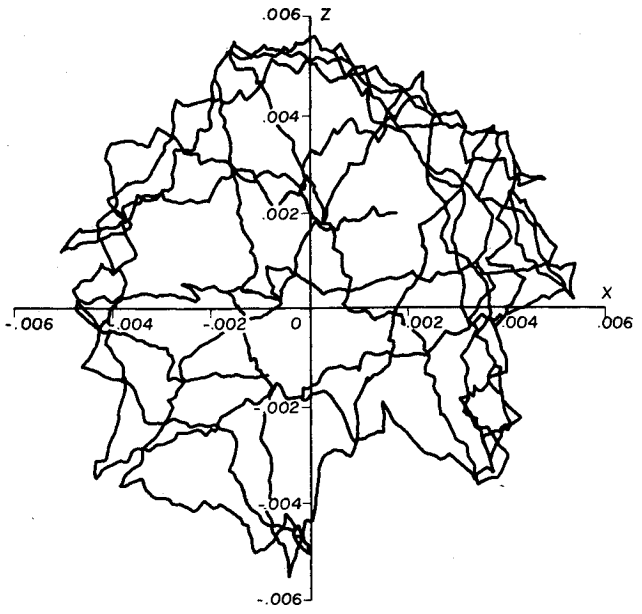

Fig. 5 Simulated acceleration errors in $x-z$ plane (mm/sec^2).

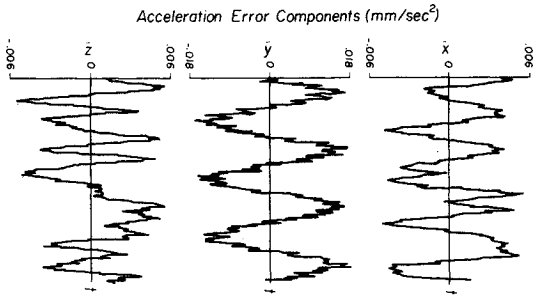

Fig. 6 Simulated acceleration error components ($t=35$ days).

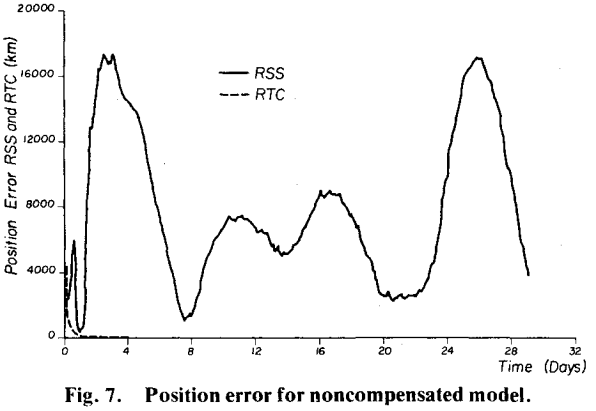

Fig. 7. Position error for noncompensated model.

forming the spacecraft initial subpoint location. The actual spacecraft initial location is near the Earth's sphere of influence, one Earth radius below the ecliptic (heliocentric X-Y plane). The initial velocity vector is oriented essentially tangential to the Earth's orbit, but directed slightly into the northern celestial hemisphere.

The nominal observation interval is a constant 50 minutes for each observation type; hence the corresponding variances are scaled to be consistent with this sampling interval. In the study, two observation models are considered. In one, the rotational dynamics of the Earth are not considered. That is, the effects of the corresponding tracking station motion are not included in the simulation, and the tracking station location coincides with the position of the point mass representing the Earth.

In the second approach, tracking stations located on the surface of the Earth at locations which coincide with the Goldstone, California; Madrid, Spain; and Woomera, Australia tracking stations were assumed. The results indicate that the rotational effects of the Earth are an important component in simulating the estimation process.

Simplified Observation Dynamics

For the initial simulations, the simple observation model which neglects the Earth's diurnal motion was used. To provide a point of reference, the orbit determination performance was obtained with no model error compensation. These results are shown in Fig. 7. Here, and in the ensuing discussions, the Euclidean norms of the error components of position (denoted as rss), are shown along with the square root of the trace of the appropriate covariance submatrix elements (denoted as rtc). From Fig. 7, it may be seen that the assumption of a perfect dynamical model results in the estimation error covariance norms (rtc) decreasing rapidly. The estimation error norms (rss) behave radically, with divergence occurring by the second day. The error in positon and velocity reach magnitudes of nearly 18,000 km, and 18 km/sec. Clearly, such performance is unacceptable.

Model 0

Figure 8 shows the position rss and rtc curves for 35 days when the thrust acceleration error is nominally assumed to be a white noise process with covariance matrix Q (Model 0). For the nonzero diagonal submatrix, U, within Q, three values are investigated:

$$U_1 = I[10^{-6} \quad 10^{-6} \quad 10^{-7}]^T \quad mm^2/\text{sec}^4$$
$$U_2 = I[10^{-4} \quad 10^{-4} \quad 10^{-5}]^T \quad mm^2/\text{sec}^4$$
$$U_3 = I[10^{-8} \quad 10^{-8} \quad 10^{-9}]^T \quad mm^2/\text{sec}^4$$

The results seem to suggest there is a tradeoff between the values of U and the accuracy obtained. For U_1, during the first 25 days reasonably accurate estimates are obtained, after which divergence occurs. Increasing U_1 by a factor of 100 to U_2 yields a slight improvement in the accuracy over the period from 9 to 24 days. Outside this interval the accuracy is degraded. For a value of $U=U_3$, which is 0.01 U_1, the reverse is approximately true: the estimate appears to be more accurate in the neighborhood of 4 days, but not so good over the 9-24 day period. After 27 days, the accuracy becomes better again, but by 35 days the performance for each value of U is again reversed: the U_3 case has the most rapid rate of divergence, while the U_2 case has the slowest. This relative state of affairs remains the same after 35 days.

It is interesting to note that in all three cases, the estimate error covariance actual increases. It is possible that this may be due, in part to the effect of the decreasing accuracy of the angular measurements. As the spacecraft recedes from Earth, the angular measurement accuracy remains constant, but the corresponding arc length increases.

Models 1 and 2

Figure 9 shows the position error norm for Models 1a, 1b, 2a, and 2b. The nonzero values of the state noise covariance matrix are for Model 1: $q_x = q_z = 3.65 \times 10^{-6}$ (mm/sec^2)^2, $q_\epsilon = 9.78 \times 10^{-16}$ (mm/sec^2)^2, and $q_\beta = 1.34 \times 10^{-6}$ (mm/sec^2)^2, $q_\eta = 1.31 \times 10^{-27}$ (mm/sec^2)^2, and $q_\beta = 5.36 \times 10^{-11}$ rad/sec^2. All four configurations give similar performance. (The a and b configurations for each model are consolidated in the figure since they are so close; from 32 days on, their separation is distinct.) Compared with Model 0, the error norm is somewhat improved for the first 10 days, and about the same to 15 days. From 15-25 days, the norm is somewhat

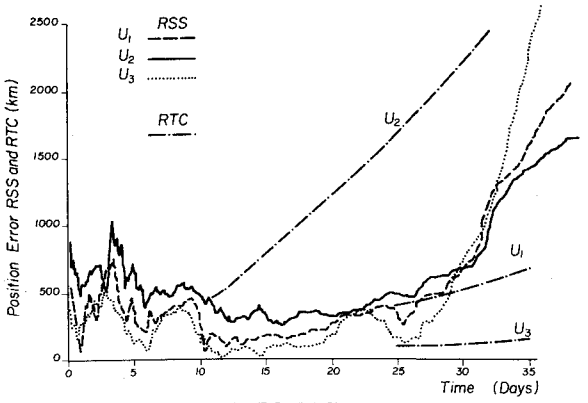

Fig. 8. Q-Matrix (Model 0) compensation.

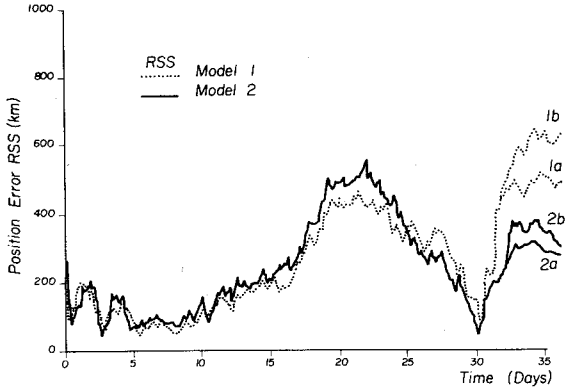

Fig. 9 First and second model performance.

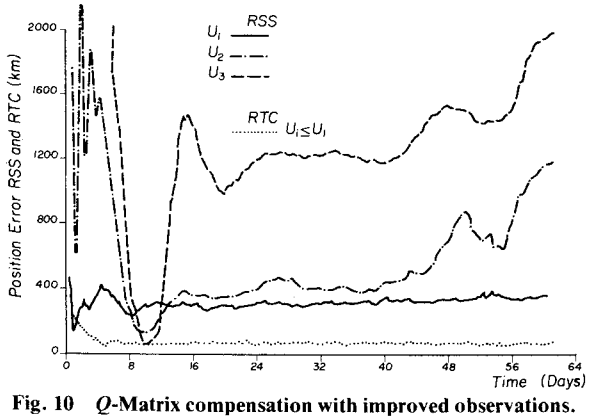

Fig. 10 Q-Matrix compensation with improved observations.

worse. After 25 days, however, divergence occurs for Model 0, while the estimate error norm remains about 400-500 km for Models 1 and 2. It is somewhat surprising and unexpected that the simpler structures (1a and 2a) yield slightly better performance.

Improved Observation Dynamics

In view of the generally poor performance described in the previous section, the oversimplification of the observation dynamics was eliminated. The results obtained when the effect of the earth's rotation is included are described in the following sections.

Model 0

A number of simulations were performed using various values of the diagonal state noise covariance matrix, U. Typical results for three linearly related values of U over a 60-day period are shown in Fig. 10. Here the estimation performance is reflected by the position error rss for the

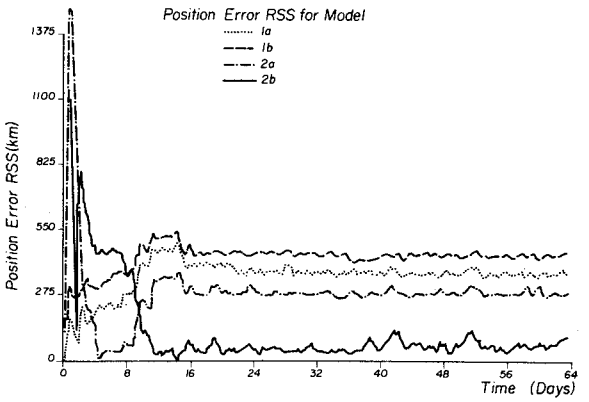

Fig. 11. Position error and covariance norms for first-and second-order models with improved observations.

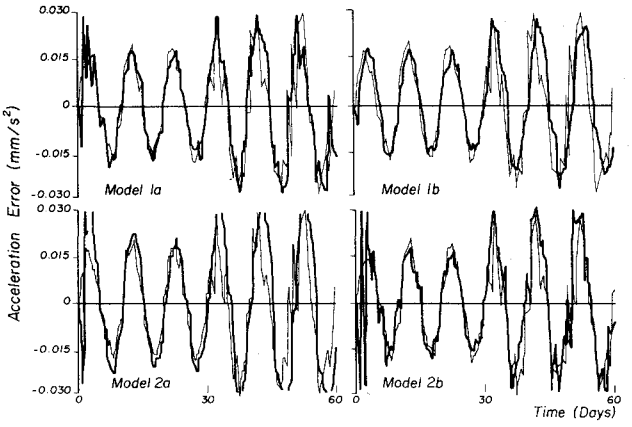

Fig. 12. Acceleration error estimate for first-and-second-order models with improved observations.

following values of U [all values in $(\text{mm/sec}^2)^2$]:

$$U_1 = I[0.16\times10^{-6}\ \ 0.166\times10^{-5}\ \ 0.16\times10^{-6}]^T$$

$$U_2 = I[0.16\times10^{-10}\ \ 0.166\times10^{-9}\ \ 0.16\times10^{-10}]^T$$

$$U_3 = I[0.16\times10^{-12}\ \ 0.166\times10^{-11}\ \ 0.16\times10^{-12}]^T$$

On examining the figure, as the state noise covariance is decreased, the tendency for divergence of the state estimate can be observed.

Again note the interesting feature of an apparent tradeoff in the values of U and the maximum estimation accuracy obtained. Here the effect is much more apparent than in Fig. 9, and is shown by the large dips in the rss curve at about 10 days. For the smallest value, U_3, the rss curve has the greatest dip; for U_1 the dip is smallest. An intuitive explanation of this phenomenon is based on the following reasoning. Initial filter operation produces estimates of greater and greater accuracy as more observations are taken. If the value of U is small, the error covariance matrix decreases rapidly, producing more nearly optimal estimates and thus, for a short time, more accurate estimates. However, eventually the covariance becomes so small that the most recent observations are not weighted properly and divergence occurs. On the other hand, for a larger U, the error covariance does not decrease as rapidly. Hence, the filter is not operating near the optimum, and estimate accuracy is therefore not as good. However, the presence of a larger U keeps the filter stable for a longer period before divergence occurs.

Next note the dotted curve which corresponds to the maximum rtc, i.e., that for U_1. Its average value is approximately 70-80 km, a value which does not reflect the error rss of 300-400 km. (Although they are not shown, the rtc's corresponding to U_2 and U_3 all lie below that for U_1.) This

suggests that the value of U_1 should be increased. The elements of U were increased to the values,

$$q_x = q_z = 0.16 \times 10^{-4} (\text{mm/sec}^2)^2$$

$$q_y = 0.16 \times 10^{-3} (\text{mm/sec})^2$$

These values lead to the values of 480 km for the position rss and 360 km for the position rtc. The position error rss is greater than that shown for U_1 in Fig. 10. However, for the increased values, the rtc curve is a better measure of the accuracy, even though it does not bound the rss curve. Further, the estimate remains fairly stable throughout the simulation period of 60 days.

Models 1 and 2

Figures 11 and 12 show the estimation performance for each of the other four approximating models. For these cases, the thrust acceleration error covariance parameters are selected to agree with the larger values discussed in the previous section. Furthermore, each case employed values of q_ℓ as indicated below.

Model 1a:

$$q_x = q_z = 0.16 \times 10^{-4} (\text{mm/sec}^2)^2$$

$$q_\epsilon = 0.16 \times 10^{-10} (\text{mm/sec}^3)^2$$

Model 1b:

$$q_x = q_z = 0.16 \times 10^{-4} (\text{mm/sec}^2)^2$$

$$q_\epsilon = 0.5 \times 10^{-14} (\text{mm/sec}^3)^2$$

$$q_\beta = 0.9 \times 10^{-35} \text{ sec}^{-4}$$

Model 2a:

$$q_x = q_z = 0.16 \times 10^{-4} (\text{mm/sec}^2)^2$$

$$q_\eta = 0.3 \times 10^{-24} (\text{mm/sec}^4)^2$$

Model 2b:

$$q_x = q_z = 0.16 \times 10^{-4} (\text{mm/sec}^2)^2$$

$$q_\eta = 10^{-22} (\text{mm/sec}^4)^2$$

$$q_\beta = 0.5 \times 10^{-30} \text{ sec}^{-6}$$

Figure 11 shows the position error rss for each of the model configurations. As expected, the estimation accuracy generally is improved over that for Model 0. The accuracy of the estimates obtained with Model 2b is quite good. This is represented by the solid curve, and corresponds to an average position rss of about 60 km for time periods greater than 10 days. This approaches a factor of 5 reduction in the rss values for the other models. It is important to remember, however, that Model 2b corresponds to a better approximation of the structure of the actual thrust acceleration error magnitude, and thus one would expect improved performance. The next most accurate performance is that provided by Model 2a, the simple linear form. As shown by the alternately dot-dashed curve, the average position rss is approximately 300 km (for time >10 days).

The two first-order models, 1a and 1b, produced acceptable but less accurate estimates. In fact, Model 1b produced a position rss curve of about 450 km, some 80 km greater than that for Model 1a. One possible reason for this is that a nonoptimal value for the state noise covariance was used. This suggestion is supported by the fact that the associated error rtc data indicated an approximately steady-state value of 280 km, a value somewhat below the actual rss curve.

For each of the other models, the indicated values of q_ℓ resulted in rtc's which coincided with or exceeded their respective rss data. The only model which produced an error rtc greater than its rss data was Model 2b. In particular, the rtc data indicated an average value of approximately 295 km.

Figure 12 shows the estimates of the y-component of the thrust acceleration for each model. These estimates are those which resulted in the estimation performances shown in Fig. 11. Each estimate of the acceleration, represented by the heavy, solid line is identified with the corresponding model number. The estimated curves are superimposed over a lighter curve, the true y-component of thrust acceleration error. As seen from Fig. 12, all four models perform well in estimating this component of acceleration error. The plots for Models 1a and 2b do not appear to be very different. On the other hand, consider the respective curves for Models 1b and 2a. Close examination of the Model 1b curve reveals that a number of the actual error peaks are not matched by the approximating curve. This is possibly due to a smaller than necessary state noise covariance matrix and presumably the estimates would be improved if these values were increased.

In view of the foregoing discussions, it appears that generally the second order Models, 2a and 2b, are superior in representing thrust acceleration errors of the type encountered in the simulations. Further, the importance of precise modeling to the extent practical is clearly illustrated by the exceptional performance of Model 2b.

VI. Conclusions

For the low-thrust navigation problem simulated in this investigation, it has been found that improved navigation may be obtained when the y-component (approximately the magnitude) of the thrust acceleration error is modeled as a first-or second-order Gauss-Markov process, and the x- and z-components treated as purely random processes. This approach yields estimates which are more accurate and considerably more stable than those obtained by assuming that all the errors are purely random. Furthermore, the second-order models give generally better performance than the first-order models.

For the formulation where the Earth's rotation is ignored, the performance is unacceptable with divergence of the state estimate eventually occurring. When the diurnal component of motion is included in the simulation the performance improves dramatically, resulting in accurate and stable long-term orbit determination estimates.

References

[1] Rourke, K. H. and Jordan, J.F., "Guidance and Navigation for Solar Electric Interplanetary Missions," *Journal of Spacecraft and Rockets,* Vol. 8, Sept. 1971, pp. 920-926.

[2] Jordan, J.F., Madriel, G.A., and Pease, G.E., "The Effects of Major-Error-Sources in Planetary Spacecraft Navigation Accuracies," *Journal of Spacecraft and Rockets,* Vol. 9, March 1972, pp. 196-204.

[3] McDanell, J.P., "Earth-Based Orbit Determination for Solar Electric Spacecraft with Application to a Comet Encke Rendezvous," AIAA Paper 73-174, Washington, D.C., Jan. 1972.

[4] Kalman, R. E. and Bucy, R.S., "New Results in Linear Filtering and Prediction," *Transactions of the ASME; Ser. D: Journal of Basic Engineering,* Vol. 82, March 1960, pp. 35-45.

[5] Jazwinski, A. H., *Stochastic Processes and Filtering Theory,* Academic Press, New York, 1969, pp. 276-277.

[6] Schlee, F. H., Standish, C.J., and Toda, N.F., "Divergence in the Kalman Filter," *AIAA Journal,* Vol. 5. June, 1967, pp. 114-1120.

[7] Tapley, B.D. and Ingram, D.S., "Orbit Determination in the Presence of Unmodeled Accelerations," *IEEE Transactions on Automatic Control,* Vol. AC-18, Aug. 1973, pp. 369-373.

[8] Ingram, D. S. and Tapley, B.D., "Lunar Orbit Determination in the Presence of Unmodeled Accelerations," ASS Paper 71-371, ASS/AIAA Astrodynamics Specialists Conference, Ft. Lauderdale, Florida, Aug. 1971.

[9] Tapley, B. D. and Schutz, B.E., "Estimation of Unmodeled Forces on a Lunar Satellite," presented at the 23rd International Astronautical Congress Vienna, Austria, Oct. 1972.

[10] Tapley, B. D. and Hagar, H., Jr., "Navigation Strategy and Filter Design for Solar Electric Missions," Rept. AMRL-1040, May 1972, Applied Mechanics Research Laboratory, The University of Texas at Austin, Austin, Texas.

[11] Hagar, Jr., H., "Model Error Compensation Techniques for Linear Filtering," AMRL Rept. 1055, Aug. 1973, Applied Mechanics Research Laboratory, The University of Texas at Austin, Austin, Texas.